

Investigating the effect of in-plane spin directions for Precessing BBH systems.

Chinmay Kalaghatgi¹ and Mark Hannam^{1,2,3}

¹*School of Physics and Astronomy, Cardiff*

²*Dipartimento di Fisica, Università di Roma “Sapienza”, Piazzale A. Moro 5, I-00185, Roma, Italy*

³*INFN Sezione di Roma, Piazzale A. Moro 5, I-00185, Roma, Italy*

(Dated: March 23, 2022)

Coalescing binary black hole (BBH) systems can be classified into non-spinning, aligned-spin and precessing systems based on the orientation of the individual black-hole (BH) spins, with the impact of spins present on the gravitational waveforms for each. Waveform models built for inference of source parameters have several in-built approximations that could induce biases on the measured source parameters. In current precessing IMRPhenom and SEOBNR waveform models, systems with the same spin magnitude but varying orientation of spins projected on the orbital plane (in-plane spin) are effectively mapped to the same system (bar an overall phase change) and the asymmetry due to precession between the $+m$ and $-m$ modes is not modelled. In this study, we investigate the validity of these approximations by generating numerical relativity (NR) simulations of single-spin NR systems with varying in-plane spin directions (including several *superkick* configurations) and provide an estimate of the SNR at which the effect of varying in-plane spin directions would be measurable. This is done computing the noise-weighted inner product (match) between these waveforms and using these match values to estimate the distinguishability SNR. We also use NR waveforms with different spin magnitudes to compare the measurability of spin magnitude vs. in-plane spin direction. We find that the in-plane spin direction *could* be measurable at SNRs accessible by current generation detectors, with the distinguishability SNR of varying in-plane spins *comparable to or lower* than varying the in-plane spin magnitude. We then remove the mode-asymmetry content from the waveforms and find that, i) removing mode-asymmetry increases the SNR at which in-plane spin direction can be measured and ii) not modelling mode-asymmetry will lead to measurement biases. The SNRs that we see at which the in-plane spins would be measurable and at which mode-asymmetric content impacts the measurements are the SNRs at which precession would be measurable [1], and we therefore conclude that modelling in-plane spin direction and mode-asymmetry effects is necessary for unbiased measurements of precession.

I. INTRODUCTION

Since the advent of the Advanced LIGO [2] and Virgo [3] gravitational-wave detectors in 2015, there have been 17 confirmed detections of binary-black-hole (BBH) mergers and one binary-neutron-star merger [4–10]. The BBH observations have begun to reveal the astrophysical rate of black-hole mergers, and the astrophysical distribution of black-hole masses and spins [11]. To measure the binary’s properties the detector data are compared against a set of theoretical model waveforms. The accuracy of the measured parameters depends not only on the details of the source, the signal-to-noise ratio (SNR), and parameter degeneracies, but also on the accuracy of the waveform models. Two families of waveform models, IMRPhenom [12–15] and SEOBNR [16–20], were used to calculate the reported parameters during the first two observation runs. Both rely on several physical approximations. In this paper we test the validity and impact of some of those approximations. (Note that a complementary study [21] considers the impact of several other modelling assumptions.)

Binary-black-hole inspiral is the result of orbital energy and angular momentum loss through gravitational radiation. If the radiation from a binary is decomposed into spin-weighted spherical harmonics, ${}^{-2}Y_{\ell m}(\theta, \phi)$, the signal is dominated by the “quadrupole” contribution in the $\ell = 2$ harmonics. Gravitational waves also carry linear momentum, and for non-spinning or aligned-spin binaries (where the black-hole spins \mathbf{S}_i are parallel to the orbital angular momentum, \mathbf{L} , so that $\mathbf{L} \times \mathbf{S}_i = 0$), the resultant recoil of the center-of-mass within the orbital plane is manifest in the signal through interplay between different multipoles; see, for example, Ref. [22]. Current aligned-spin binary waveform models that include higher multipoles capture all of these physical effects, with varying degrees of accuracy, Ref. [13, 17, 23]. In generic binaries,

where the spins are mis-aligned with the orbital angular momentum, the orbital plane and spins precess during the inspiral. Generic binaries also radiate linear momentum perpendicular to the orbital plane. This effect, which shows up in the GW signal through an asymmetry between the $+m$ and $-m$ multipoles, is not present in current precessing SEOB [24] and Phenom [25] models. Although these models include the spin directions while computing the precession angles, the effect of varying spin-directions on the full waveforms remains un-modelled due to the use of the corresponding aligned-spin waveform in the co-precessing frame. Our goal is to make a first estimate of the effect of these omissions on GW source parameter measurements.

We begin by describing in more detail the phenomenology of BBH systems, and the construction of generic-binary waveform models.

A BBH system undergoing non-eccentric inspiral can be characterised by eight parameters, the individual masses (m_i), and the components of the two spin vectors (\mathbf{S}_i), specified at some fiducial point during the inspiral, for example a chosen orbital frequency. The GW signal is also parameterised by the binary’s sky-position (α, δ), inclination (ι), coalescence phase (ϕ_c), distance (d_L), polarisation (ψ) and time of arrival (t_c) at the detector. As noted above, the complex GW strain can be decomposed into spin-weighted spherical harmonics as,

$$h(t, \theta, \phi) = h_+(t) - ih_\times(t) = \sum_{\ell, m} h_{\ell m}(t) {}^{-2}Y_{\ell m}(\theta, \phi), \quad (1)$$

where (θ, ϕ) give the position of the observer on a sphere centred on the centre-of-mass of the binary.

Based on the black-hole (BH) spin configurations, coalescing BBH systems with spins can be considered to be either:

- **Aligned-Spin:** The BH spins are parallel or anti-parallel to \mathbf{L} , so $\mathbf{L} \times \mathbf{S}_i = 0$, where $i = 1, 2$ for each

BH. From the symmetries of the system, the BHs orbit in a fixed plane, i.e., the direction of the orbital angular momentum $\hat{\mathbf{L}}$ remains fixed. In the frame where $\hat{\mathbf{L}} \parallel \hat{\mathbf{z}}$, symmetry also implies that

$$h_{\ell,m} = (-1)^{\ell} h_{\ell,-m}^*, \quad (2)$$

and that any linear momentum emission is perpendicular to \mathbf{L} ; although the orientation of the orbital plane remains fixed, the center-of-mass can recoil within this plane.

- **Precessing:** One or both BHs have non-zero spin components perpendicular to $\hat{\mathbf{L}}$. We denote the parallel components by \mathbf{S}_i^{\parallel} and the perpendicular components by \mathbf{S}_i^{\perp} . The presence of \mathbf{S}_i^{\perp} causes the orbital plane to precess over the course of the coalescence. This leads to modulations of the amplitude and phase of the waveform. Emission of linear momentum is now also possible perpendicular to the orbital plane, which breaks the symmetry of Eq. (2) between the $\pm m$ multipoles.

As was shown in previous studies [26–28], a precessing waveform can be decomposed into the waveform as observed in a co-precessing frame, h^{CP} , and a time- or frequency-dependent rotation that describes the precessional dynamics. The rotation can be expressed in terms of three Euler angles, (α, β, γ) , and the $\ell = 2$ modes of the precessing-binary waveform h^{P} constructed as

$$h_{2m}^{\text{P}} = e^{im\alpha} \sum_{m'} e^{-im'\epsilon} d_{mm'}^2(\beta) h_{2m'}^{\text{CP}}, \quad (3)$$

where $d_{mm'}^2$ denote the $\ell = 2$ Wigner-d matrices. In the current precessing models (IMRPhenom and SEOBNR), the co-precessing-frame waveform is based on an underlying non-precessing-binary model (with some modifications), and this procedure preserves its orbital-plane symmetry, Eq. (2). These models therefore do not include the $\pm m$ mode asymmetry of full precessing-binary waveforms.

The magnitude and direction of the out-of-plane angular momentum loss \dot{p}_{\parallel} (and therefore the level of mode asymmetry) is related to the angles between the in-plane spins \mathbf{S}_i^{\perp} and the separation vector between the two black holes $\hat{\mathbf{n}}$, as most easily seen in the PN treatment in Sec. III E of Ref. [29]. During one orbit the spin directions change little, so \dot{p}_{\parallel} oscillates approximately on the orbital timescale. In the “twisted-up” models described above, this effect is not present, and an overall rotation of the spin(s) in the orbital plane introduces only an offset in the precession angle α , which is degenerate with the azimuthal angle, ϕ , since it enters the spin-weighted spherical harmonics as $e^{im\phi}$. The model waveforms are therefore degenerate with respect to a constant rotation of the in-plane spins, while true waveforms include an additional effect that varies sinusoidally with respect to this spin rotation.

Out of plane recoil in the context of mode asymmetries has been discussed in NR simulations in [30], and further illustration of the effect in GW signals is shown in [21]. Earlier studies on in-plane effects on waveforms and/or mode-asymmetries for precessing systems include [31–33].

In this study, we investigate the effects of varying the in-plane spin direction for single-spin precessing NR waveforms for a given combination of mass-ratio and spin. We also consider the special case of the “super-kick” configuration [30, 34, 35]: these are equal-spin configurations where

the spins lie entirely in the orbital plane, and $\mathbf{S}_1 = -\mathbf{S}_2$. Due to the symmetry of this configuration, the orbital plane does not precess, but *does* bob up and down due to linear momentum loss, making this an especially clean system for the study of mode asymmetry. We choose these configurations to estimate the importance of mode-asymmetric content on parameter measurements. Using the waveform with in-plane spin aligned to the position vector as a *proxy template*, we compute matches against systems with other in-plane spin directions. Using a relationship between the match value and SNR at which two signals are distinguishable, we provide an estimate of the SNR at which mode asymmetries will impact parameter measurements. We also use a selection of waveforms with the same spin direction as the proxy template but with differing in-plane spin magnitude to estimate the relative strength of the effect of varying spin direction versus varying spin magnitude.

The paper is organised as follows. Sec. II provides details of the simulations generated for this study. Sec. III A and Sec. III B discuss the computation of precessing matches and the connection between the match and detectable SNR respectively. The setup for the study is explained in Sec. IV with the results in Sec. V. The conclusions we draw from this work, and some of its limitations and potential future extensions, are discussed in Sec. VI.

II. NR WAVEFORMS

For this study, a set of 12 new NR simulations were performed with the BAM code [36, 37]. Configurations are defined by the mass ratio, $q = m_2/m_1$, where we choose the convention $m_2 > m_1$, and the spin vectors specified at the start of the simulation, \mathbf{S}_i . In the unequal-mass simulations, only the larger black hole is spinning, so that $\mathbf{S}_1 = 0$. For these simulations we can completely specify the spin direction at the beginning of the simulation by two angles, i) the angle between the spin vector and angular momentum vector, which we call θ_{SL} , and ii) the angle between the separation vector ($\hat{\mathbf{n}}$) and the projection of spin onto the orbital plane (\mathbf{S}_i^{\perp}), which we call ϕ_{Sn} . The codes available for initial data generation did not allow for user specified $(\theta_{SL}, \phi_{\text{Sn}})$ values and so a novel method was developed for obtaining the required initial data for single-spin precessing systems. We describe the initial data generation method in Section: II A and provide the details of the simulations in Section: II B.

A. Initial data generation

For this study, we required single-spin precessing NR waveforms with user specified $(\theta_{SL}, \phi_{\text{Sn}})$ at a given reference frequency $M\omega_{\text{orb}}$. Over the course of inspiral, the spin vectors of a precessing system oscillate about a mean value with the oscillation frequency increasing as system nears merger [38]. An iterative method was required to ensure the required spin direction at the given reference frequency. The code used for solving the PN equations was one which was used for BAM NR waveforms as used in [26, 39, 40]. The method developed for initial data generation is as below. The PN evolution is started in the $\vec{\mathcal{J}}$ aligned to $\hat{\mathbf{z}}$ frame with $\vec{\mathcal{L}}$ being the Newtonian

Config	q	\vec{S}_2	$\vec{r} = D/M$	$\vec{p} = \vec{p}_1 - \vec{p}_2$	$\omega_{start}(fM)$	ϕ_{Sn}	θ_{SL}
q1a08p0 _{sk}	1	(0, -0.799, -0.001)	(0, 11.623, 0)	(-0.174, -0.001, 0)	0.0225	0	$\pi/2$
q1a08p90 _{sk}	1	(0.7999, 0, -0.0012)	(0, 11.623, 0)	(-0.174, -0.001, 0)	0.0225	$\pi/2$	$\pi/2$
q1a08p180 _{sk}	1	(0, 0.7999, -0.0012)	(0, 11.623, 0)	(-0.174, -0.001, 0)	0.0225	π	$\pi/2$
q1a08p270 _{sk}	1	(-0.7999, 0, -0.0012)	(0, 11.623, 0)	(-0.174, -0.001, 0)	0.0225	$3\pi/2$	$\pi/2$
q2a07p0	2	(-0.001, 0.699, 0.006)	(0., 10.810, 0.)	(-0.105, -0.001, 0.123)	0.025	0	$\pi/2$
q2a07p90	2	(-0.451, -0.005, 0.535)	(0., 10.810, 0.)	(-0.105, -0.001, 0.123)	0.025	$\pi/2$	$\pi/2$
q2a07p180	2	(0.006, -0.699, -0.002)	(0., 10.810, 0.)	(-0.105, -0.001, 0.123)	0.025	π	$\pi/2$
q2a07p270	2	(0.448, -0.005, -0.537)	(0., 10.810, 0.)	(-0.105, -0.001, 0.123)	0.025	$3\pi/2$	$\pi/2$
q4a08p0	4	(0.0007, 0.799, -0.005)	(0., 11.486, 0.)	(-0.111, -0.0004, 0.014)	0.0225	0	$\pi/2$
q4a08p90	4	(-0.793, 0, 0.099)	(0., 11.486, 0.)	(-0.111, -0.0005, 0.014)	0.0225	$\pi/2$	$\pi/2$
q4a08p180	4	(-0.0007, -0.799, -0.005)	(0., 11.486, 0.)	(-0.111, -0.0004, 0.014)	0.0225	π	$\pi/2$
q4a08p270	4	(0.792, 0, -0.110)	(0., 11.486, 0.)	(-0.111, -0.0005, 0.0147)	0.0225	$3\pi/2$	$\pi/2$
q4a04p0	4	(-0.001, 0.399, -0.00007)	(0., 11.486, 0.)	(-0.111, -0.0004, 0.014)	0.0299	0	$\pi/2$
q2a04p0	2	(-0.00008, 0.3999, -0.0008)	(0., 11.6299, 0.)	(-0.153, -0.0009, 0.015)	0.0224	0	$\pi/2$
q2a08p0	2	(0.0005, 0.799, -0.003)	(0., 11.5709, 0.)	(-0.153, -0.0009, -0.0243)	0.023	0	$\pi/2$

Table I. Table of NR simulations used for this study. From left to right, the columns show the name of the simulation, the mass-ratio of the system, value of the spin on the larger black hole at the reference frequency, the separation between the black holes at the reference frequency, the total momenta of the system at the reference frequency, the reference frequency at which the simulation starts, and the values of the ϕ_{Sn} and θ_{SL} angles respectively. For the $q = 1$ series, note that $\mathbf{S}_2 = -\mathbf{S}_1$.

angular momentum.

The angle between the spin vector and angular momentum vector, (θ_{SL}), varies not more than $\sim 1^\circ$ over the inspiral phase. Hence, once (θ_{SL}) is specified, further iteration is not required. To obtain the required ϕ_{Sn} , the algorithm goes through the following steps:

Step 1:

This step consists of two iterations.

Iteration 1: Initially, both the BHs are placed along the x-axis with a given separation, the orbital plane is the x - y plane, and the initial spin (\mathbf{S}_{ini}) parallel to \hat{n} . The spin vector is then rotated to obtain the required θ_{SL} and the PN evolution code is run until $M\omega_{orb}$ is reached. We record the time when the specified orbital frequency is reached (t_0), the value of $\phi_{Sn}(t)$ at t_0 [$\phi_{Sn}(t_0)$], the closest time to t_0 at which $\phi_{Sn}(t) = \phi_{Sn}^{target}$, which is denoted t_1 , and finally the relative frequency error (ω_{err}) between the orbital frequencies at t_0 and t_1 . If, at this iteration, ϕ_{Sn} at t_0 is not ϕ_{Sn}^{target} or if ω_{err} is larger than a pre-specified threshold (ω_{err}^F), the value of $\phi_{Sn}^{t_1}$ is recorded; we call this ϕ_{Sn}^1 . Each iteration hence also stores the value $\phi_{Sn}^{t_0, i}$. For these simulations, we use $\omega_{err}^F = 1\%$.

Iteration 2: During iteration 2, \mathbf{S}_{ini} is rotated to obtain the required θ_{SL} and then further rotated by $(-\phi_{Sn}^1)$ about the z -axis, and then the PN solver is again run. If the conditions specified in Iteration 1 are met ($\omega_{err} < \omega_{err}^F$ & $\phi_{Sn}^{t_1} = \phi_{Sn}^{target}$) then the parameters at t_1 are recorded. If not, we would ideally simply repeat the process. However, since ϕ_{Sn} changes on the (rapid) orbital timescale, the value of ϕ_{Sn} at the NR reference frequency is very sensitive to the choice at the beginning of the PN evolution, and so this procedure is not well-conditioned to fine-tune ϕ_{Sn} . We instead proceed to Step Two, and store the value of $\phi_{Sn}^{t_1}$ of this iteration as ϕ_{Sn}^2 .

Step 2: Depending on the parameters, this step can consist of one or multiple iterations. For each iteration, \mathbf{S}_{ini} is rotated to obtain the required θ_{SL} and then by the specified $-\phi_{rot}$ about \hat{z} .

Iteration 3: For each iteration hence, we define a angle correction parameter, ϕ_{corr} . $\omega_{err} - \omega_{err}^F$ gives an idea of how

close we are to the required initial parameters and value of ϕ_{corr} is based on that. If, $\omega_{err} - \omega_{err}^F > \frac{1}{2}\omega_{err}^F$, then $\phi_{corr} = 10^\circ$, else $\phi_{corr} = 5^\circ$ and then $\phi_{rot} = \phi_{Sn}^2 + \phi_{corr}$. Using these angles, the spin is rotated and PN solver is run. Again, the value of $\phi_{Sn}^{t_1}$ of this iteration as ϕ_{Sn}^3 .

Iteration $n > 3$: First, we check if $\phi_{Sn}^3 > \phi_{Sn}^2$. If so, the initial spin is being rotated in the wrong direction and for each subsequent iteration, $\phi_{rot} = \phi_{Sn}^2 - (n-3) \times \phi_{corr}$, if not, $\phi_{rot} = \phi_{Sn}^2 + (n-2) \times \phi_{corr}$. Thus, we brute force the initial direction of \mathbf{S}_{ini} until the required direction of \mathbf{S} is obtained at the reference frequency.

To apply this procedure with a higher tolerance, one should reduce ϕ_{corr} in subsequent iterations. For the simulations produced here, no more than two or three iterations in Step Two were required.

B. Details of the Simulations

The simulations are split into three sets based on the mass-ratio of the system: $q = 2$, $q = 4$ and a super-kick series at $q = 1$.

The $q = 2$ series is a set of four $q = 2$ NR waveforms with a total in-plane spin of dimensionless magnitude $\chi_2 = S_2/m_2^2 = 0.7$, with $\theta_{SL} = \pi/2$ and $\phi_{Sn} = (0, \pi/2, \pi, 3\pi/2)$. For the $q = 4$ series we use $\chi_2 = 0.8$ and the same (θ_{SL}, ϕ_{Sn}) configurations as for the $q = 2$ series.

The $q = 1$ simulations are two-spin systems in the “super-kick” configuration, where both black holes are spinning, with equal and opposite in-plane spins of $\chi_i = 0.8$. The super-kick configurations are non-precessing and due to the symmetry of the system, the final recoil is along $\pm \hat{z}$.

For the simulation names, the following convention is used: q(mass-ratio of system)a(total spin of system)p(value of ϕ_{Sn}), following which, the first simulation in the $q = 2$ series is q2a07p0. The angle, θ_{SL} , between \hat{L} and \hat{S} is always $\pi/2$ for these systems, i.e., $\mathbf{S}_i^\parallel = 0$. For the $q = 1$ series waveforms, remember that the total spin satisfies $\mathbf{S}_1 + \mathbf{S}_2 = 0$,

but we follow the above naming convention naming with "sk" in subscript for simplicity. We also use three extra NR simulations with different total in-plane spin values (with same θ_{SL} and $\phi_{Sn} = 0$), which are used as comparison cases, and were produced as part of the waveform catalogue presented in Ref. [41].

Initial momenta consistent with low-eccentricity inspiral were estimated using the PN/EOB evolution code described in Refs. [39, 40, 42]. We perform a short simulation of less than $1000M$ duration, and estimate the eccentricity from the co-ordinate separation, as given in Eq. (3) of Ref. [43]. For the $q = 2$ and $q = 1$ series, the eccentricities were all $< 5 \times 10^{-3}$, and we used the same initial momenta for production simulations. For the $q = 4$ configurations, however, further eccentricity reduction was required.

Ref. [42] describes an efficient procedure to further reduce eccentricity for non-precessing binaries. For the precessing simulations used here, we adopted a simpler procedure: we performed a series of simulations with momenta increased or reduced by multiples of 0.1%, until an eccentricity below our threshold was obtained. For the q4a08p0 configuration, the original momenta estimate was reduced by 0.1%, and for the q4a08p90 configuration it was increased by 0.25%. Note that the eccentricity for a system with $\phi_{Sn} \rightarrow \phi_{Sn} \pm \pi$ has the same value.

For the $q = 2$ series, once the parameters for the $\phi_{Sn} = 0$ configuration were obtained, the parameters for the other simulations in the series were obtained simply by rotating the initial spin in the plane; the resulting eccentricities were all within our tolerance. For the $q = 4$ and $q = 1$ series, however, the initial-parameter code was run separately for each value of ϕ_{Sn} .

BAM's mesh-refinement scheme is constructed as described in Refs. [36, 37]. In particular, a nested set of boxes centred on each black hole. For each simulation in this series, the boxes around the BHs consisted of 80 points in each direction, with a grid-spacing on the finest level of $m_1/56$, $m_1/36$ and $m_1/44$ for the $q = 1$, $q = 2$ and $q = 4$ series respectively. Further details of the grid setups are provided in Ref. [41]. For two of the cases (q2a07p0 and q2a07p90), we performed higher-resolution runs with 96-point boxes, and a finest-level resolution of $m_1/48$. Using these two waveforms, we computed the match between the different resolution runs over a range of (θ, ϕ) values (see Eq. (1)) using only the $l = 2$ modes (as these are the modes used throughout the paper). We find that over the range of (θ, ϕ) values considered, we obtain matches of $\sim 0.9995 - 0.99995$. This shows that using the 96 point runs will not qualitatively change our results, but we will discuss this in more detail in Sec. IV; see discussion pertaining to Fig. 1.

III. ANALYSIS METHODS

This section provides the details of the match computation procedure employed for computing matches between the various precessing waveforms and the connection between the match and the SNR at which the template and signal can be distinguished from each other. This is the primary method we use to interpret the results in Sec. V.

A. Match computations

For the given physical system (with fixed intrinsic parameters), the detector response is uniquely determined by the systems sky-position, inclination (i), coalescence-phase (ϕ_c), polarisation (ψ) and time of arrival (t_c). The degree of agreement between two gravitational waveforms can be ascertained by computing the match, \mathcal{M} , between the two waveforms. A value of $\mathcal{M} = 1$ implies the waveforms are in perfect agreement. The smaller the value of \mathcal{M} , the larger the disagreement between the two waveforms. The match computation we give follows Appendix B of Ref. [38].

For a GW source directly overhead the detector, i.e., $(\alpha, \delta) = (0, 0)$, the real valued detector response ($h_{det}(t, \vec{\lambda})$), in terms of the two gravitational wave polarisations is,

$$h_{det}(t, \vec{\lambda}) = h_+ \cos(2\psi) + h_\times \sin(2\psi) = \text{Re} [h(t, \vec{\lambda}) e^{2i\psi}], \quad (4)$$

with h_+ and h_\times as defined in Eq. (1). Here, due to $(\alpha, \delta) = (0, 0)$, the individual detector response depends only on ψ .

A Fourier transform of the detector response gives us the frequency domain response, which can be written as,

$$h_{det}(f, \vec{\lambda}) = \frac{1}{2} [h(f) e^{2i\psi} + h^*(-f) e^{-2i\psi}]. \quad (5)$$

The match between two waveforms, a signal waveform, $\tilde{h}_s(f, \vec{\lambda})$, and template waveform, $\tilde{h}_t(f, \vec{\lambda})$, is given by the noise-weighted inner product between the two,

$$\mathcal{M}(\tilde{h}_s(f, \vec{\lambda}), \tilde{h}_t(f, \vec{\lambda})) = \langle \tilde{h}_s(f) | \tilde{h}_t(f) \rangle, \quad (6)$$

where the noise-weighted inner product is defined as,

$$\langle a | b \rangle = 4 \text{Re} \left[\int_{-\infty}^{\infty} \frac{\tilde{a}(f) \tilde{b}^*(f)}{S_n(f)} df \right]. \quad (7)$$

Combining Eqs. (5), (6) and (7) gives us the inner product between two waveforms as,

$$\begin{aligned} \langle \tilde{h}_s(f) | \tilde{h}_t(f) \rangle &= \text{Re} \int_{-\infty}^{\infty} \frac{\tilde{h}_s(f) \tilde{h}_t^*(f)}{S_n(f)} e^{2i(\psi-\sigma)} df + \\ &\quad \text{Re} \int_{-\infty}^{\infty} \frac{\tilde{h}_s(f) \tilde{h}_t^*(-f)}{S_n(f)} e^{2i(\psi+\sigma)} df, \end{aligned} \quad (8)$$

where ψ and σ are the polarisation values of the signal and template, respectively. We can rewrite Eq. (8) as,

$$\langle \tilde{h}_s(f) | \tilde{h}_t(f) \rangle = \text{Re} \int_{-\infty}^{\infty} \frac{\tilde{h}_t^*(f) e^{-2i\sigma}}{S_n(f)} [\tilde{h}_s(f) e^{2i\psi} + \tilde{h}_s^*(-f) e^{-2i\psi}]. \quad (9)$$

As we want to compute the normalized matches, we first need to obtain the norm of the signal waveform. Using Eq. (8),

$$\begin{aligned} \|\tilde{h}_s(f, \vec{\lambda})\|^2 &= \text{Re} \int_{-\infty}^{\infty} \frac{\tilde{h}_s(f) \tilde{h}_s^*(f)}{S_n(f)} df + \\ &\quad \text{Re} \int_{-\infty}^{\infty} \frac{\tilde{h}_s(f) \tilde{h}_s^*(-f)}{S_n(f)} e^{4i\psi} df. \end{aligned} \quad (10)$$

Now, we need the normalized match optimized over template polarisation. To do that, we first define a few quantities,

$$N_1 = \int_{-\infty}^{\infty} \frac{|\tilde{h}_t(f)|^2}{S_n(f)} df, \quad N_2 e^{i\sigma_n} = \int_{-\infty}^{\infty} \frac{\tilde{h}_t(f) \tilde{h}_t^*(-f)}{S_n(f)} df. \quad (11)$$

Using the form of Eq. (10) and the terms from Eq. (11), the template norm can be written as,

$$|\tilde{h}_t(f)|^2 = N_1 + N_2 \cos(\sigma_n + 4\sigma). \quad (12)$$

Next, we define,

$$Me^{i\sigma_m} = \int_{-\infty}^{\infty} \frac{\tilde{h}_t^*(f)}{S_n(|f|)} [\tilde{h}_s(f)e^{2i\psi} + \tilde{h}_s^*(-f)e^{-2i\psi}], \quad (13)$$

which allows us to rewrite Eq. (9) as,

$$\langle \tilde{h}_s(f) | \tilde{h}_t(f) \rangle = M \cos(\sigma_m - 2\sigma). \quad (14)$$

Using the above definitions, we can write the normalized match maximised over template polarisation as,

$$\begin{aligned} \max_{\sigma} \left\langle \frac{h_s(\tilde{f})}{\|h_s(\tilde{f})\|} \middle| \frac{h_t(\tilde{f})}{\|h_t(\tilde{f})\|} \right\rangle &= \max_{\sigma} \frac{M}{\|h_s(\tilde{f})\|} \frac{\cos(\sigma_m - 2\sigma)}{\sqrt{N_1 + N_2 \cos(\sigma_n + 4\sigma)}} \\ &= \frac{M}{\|h_s(\tilde{f})\|} \sqrt{\frac{N_1 - N_2 \cos(\sigma_n + 2\sigma_m)}{N_1^2 - N_2^2}}. \end{aligned} \quad (15)$$

Given a template and signal waveform with given signal polarisation, Eq. (15) gives the match optimized over template polarisation.

B. Confidence intervals from match values

Let the detector data $d(t)$ with noise $n(t)$ have a signal $h(t, \vec{\lambda}_0)$ present, giving us,

$$d(t) = h(t, \vec{\lambda}_0) + n(t), \quad (16)$$

where $\vec{\lambda}_0$ is the vector of source parameters.

Any GW signal $h(t, \vec{\lambda})$ with $\vec{\lambda} \sim \vec{\lambda}_0$ can be Taylor expanded in terms of parameters,

$$h(t, \vec{\lambda}) = h(t, \vec{\lambda}_0) + \lambda^i \partial_i h(t), \quad (17)$$

with $\partial_i h(t)$ being the partial derivative of $h(t)$ w.r.t parameter λ_i .

Given the detector data and a waveform template, we can write the likelihood for a given set of $\vec{\lambda}$ as,

$$p(d|\vec{\lambda}) \propto \exp \left\{ -\frac{\langle d(t) - h(t, \vec{\lambda}) | d(t) - h(t, \vec{\lambda}) \rangle}{2} \right\}. \quad (18)$$

Substituting Eq. (16) for $d(t)$ and Eq. (17) for $h(t, \vec{\lambda})$ in Eq. (18), and keeping terms up to first order in λ_i ,

$$p(d|\vec{\lambda}) \propto \exp \left\{ -\frac{\langle n(t) | n(t) \rangle}{2} + \lambda_i \langle n | \partial_i h(t) \rangle - \lambda_i \lambda_j \langle \partial_i h(t) | \partial_j h(t) \rangle \right\}. \quad (19)$$

Given a likelihood, within Bayesian analysis, the posterior probability is,

$$p(\vec{\lambda}|d(t)) \propto p(d|\vec{\lambda})p(\vec{\lambda}), \quad (20)$$

where $p(\vec{\lambda})$ is the prior over the parameters, which can be assumed to be flat for detectable signals. The flat prior assumption, although not physically motivated, is a reasonable

approximation as the likelihood function would be highly peaked in a very small region of the full parameter space.

Once we have a posterior distribution, we can define a region in parameter space (Θ) that contains a given probability p of the posterior distribution,

$$p = \int_{\Theta} d\lambda p(\vec{\lambda}|d). \quad (21)$$

Such confidence intervals can be computed by obtaining the posteriors from a full parameter estimation computation, but here we will derive the confidence intervals within the Fisher matrix approximation.

Before computing the confidence intervals, we would like to point out the expressions for mean ($\langle \lambda_i \rangle$) and variance ($\langle \lambda_i \lambda_j \rangle$) of given parameters,

$$\langle \lambda_i \rangle = \int d\lambda p(\vec{\lambda}|d(t)) \langle \partial_i h | \partial_j h \rangle^{-1} \langle n | \partial_j h \rangle, \quad (22)$$

$$\langle \lambda_i \lambda_j \rangle = \langle \partial_i h | \partial_j h \rangle^{-1}. \quad (23)$$

Using the above expressions along with Eq. (19) and the assumption of a flat prior, we can re-express the posterior distribution Eq. (20) as,

$$\begin{aligned} p(\vec{\lambda}|d(t)) &\propto \exp \left\{ -\frac{1}{2} \langle \lambda_i - \langle \lambda_i \rangle | \langle \partial_i h | \partial_j h \rangle^{-1} \langle \lambda_j - \langle \lambda_j \rangle \rangle \right\} \\ &\sim \exp \left\{ -\frac{1}{2} \langle h(\vec{\lambda}) - h(\langle \vec{\lambda} \rangle) |^2 \right\}. \end{aligned} \quad (24)$$

The region that contains a given probability p of the posterior distribution is the one where,

$$|h(\vec{\lambda}) - h(\langle \vec{\lambda} \rangle)|^2 < \chi_k^2(1 - p), \quad (25)$$

where $\chi_k^2(1 - p)$ is the chi-square value wherein there is probability $(1 - p)$ of obtaining the given value or larger with k being the number of dimensions for the problem.

For two waveforms close to each other in the parameter space, i.e., for $h_1(\vec{\lambda}_1)$ and $h_2(\vec{\lambda}_2)$ with $\vec{\lambda}_1 \sim \vec{\lambda}_2$, and, $|h_1|^2 \sim |h_2|^2 \sim \rho^2$ with ρ being the SNR of the signal:

$$|h_1(\vec{\lambda}_1) - h_2(\vec{\lambda}_2)|^2 = 2|h_1|^2 \left[1 - \frac{\langle h_1 | h_2 \rangle}{|h_1||h_2|} \right] \sim 2\rho^2[1 - \mathcal{M}]. \quad (26)$$

This gives a condition on confidence intervals in terms of match values as,

$$\mathcal{M}[h_1, h_2] \geq 1 - \frac{\chi_k^2(1 - p)}{2\rho^2}. \quad (27)$$

Two waveforms would be distinguishable from each other if the posteriors recovered for the two have different confidence intervals. So, given a match value, the above gives us a condition for the SNR at which the waveforms would be distinguishable,

$$\rho \geq \sqrt{\frac{\chi_k^2(1 - p)}{2(1 - \mathcal{M})}}. \quad (28)$$

For the systems under consideration, there are a total of 7 parameters which can be varied and hence, $k = 7$. At $k = 7$ for 90% confidence intervals, $\chi_k^2(1 - p) = 12.02$.

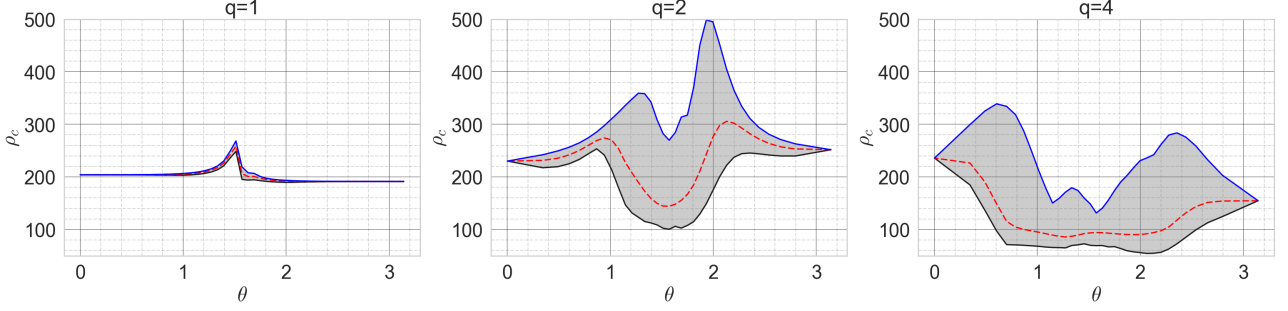


Figure 1. The left, middle and right columns show ρ_c for signals q1a08p180_{sk}, q2a07p180, and q4a08p180 respectively, as seen by templates q1a08p0_{sk}, q2a07p0 and q4a08p0, across the signal θ space. For each signal θ , the match is computed with the template at $\theta + \pi$, over a range of ϕ values, and the black, dashed-red and blue lines show the minimum, mean and maximum match (ρ_c) across the ϕ space. We observe a larger variation of ρ_c for the $q = 2$ and $q = 4$ cases as compared to the $q = 1$ due to presence of non-zero subdominant modes, $(l, m) = (2, 1)$, $(2, 0)$ and $(2, -1)$. As mentioned in Sec. II, the matches between 80 and 96 point runs were $\sim 0.9995 - 0.99995$, which translates to $\rho_c \sim 110 - 350$, with the lower matches near $\theta \sim \pi/2$ and higher matches towards $\theta \sim 0, \pi$. Hence, all results should be accurate up to $\rho_c \sim 110$ within NR accuracy. Note that the initial data for $q = 4$ series were obtained individually and hence have slightly different momenta, which is one of the reasons for their low ρ_c .

The above discussion was as given in Ref. [44], although previous studies [45–49] have used similar definitions to determine the distinguishability/accuracy requirements of gravitational waveforms. As was pointed out in [50], the equality in Eq. 28 is a sufficient, but not always a necessary condition, to determine the accuracy between two waveforms. If the above condition is not satisfied, biases *may* arise during parameter inference and so, the above equality is a conservative estimate of accuracy requirements.

IV. SETUP

To reiterate, the aim of this study is to investigate the distinguishability of systems with varying directions of the in-plane spin and the impact of mode-asymmetry on the same. To do that, we will use the $\phi_{\text{Sn}} = 0$ system from each of the $q = 1$, $q = 2$ and $q = 4$ series of NR simulations as the *proxy* template and use the other waveforms in each series as the signal waveforms. For the match computations, the signal is recomposed from only the $\ell = 2$ modes using Eq. (1) and Eq. (4). Each signal is uniquely defined by its inclination (θ^s), phase (ϕ^s) and polarisation (ψ^s)¹. For each unique signal, the match is maximised over the template $(\theta^t, \phi^t, \psi^t)$. A total mass of $100M_\odot$ is used for both signals and templates and the match is computed with $(f_{\text{min}}, f_{\text{max}}) \in (20, 600)$ Hz for the results presented in Section IV and Section V A.

For the results below, the signals (θ^s, ϕ^s) are isotropically distributed over a sphere with 30 points in θ^s and 25 points in ϕ^s . For each signal (θ^s, ϕ^s) , we choose four values of $\psi^s \in [0, \pi/2]$ and then maximise the match over the template $(\theta^t, \phi^t, \psi^t)$. The match maximisation procedure goes through the following four steps,

- Isotropically grid the template (θ^t, ϕ^t) space over the sphere with 41 points in θ^t and 81 points in ϕ^t .

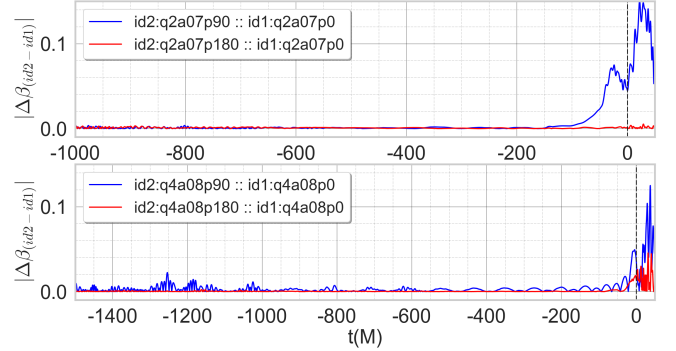


Figure 2. Blue lines show the differences in the β Euler-angle (in radians) between the $\phi_{\text{Sn}} = 0, \pi/2$ systems for $q = 2$ (upper panel) and $q = 4$ (lower panel) series. Red lines show the same for the $\phi_{\text{Sn}} = 0, \pi$ systems. For both systems, $\Delta\beta$ is small during late-inspiral, with the majority of differences arising near merger.

- For each value of template θ_i^t , we compute the match across template ϕ_j^t . For each (θ_i^t, ϕ_j^t) combination, the code gives the match optimized over template ψ^t .
- For each θ_i^t , the match is interpolated over the ϕ_j^t values, from which the maximum match over ϕ^t for each θ_i^t is obtained.
- Thus, we get a set of match values across the template θ_i^t values, which are then interpolated to obtain the maximum match over template $(\theta^t, \phi^t, \psi^t)$.

The choice of 41×81 grid for the template waveforms for match maximisation was chosen based balancing the i) accuracy of final result and ii) amount of time required for each match computation. Using some random signal (θ, ϕ) values, we found that doubling the grid size changed the results by less than 5%.

Hence, for each signal system, we have $(25 \times 30 \times 4 = 3000)$ match values. We also store the optimal SNR for each signal. In general we wish to know how easily two configurations can be distinguished for different choices of binary orientation,

¹ Note that we are considering the sky-position of the system to be exactly overhead the detector. Hence the angles (θ, ϕ) can be interpreted as the inclination and phase w.r.t the detector.

(θ, ϕ) . To average across different choices of signal polarisation, ψ^s , we follow Refs. [15, 51, 52] and average the match for each (θ^s, ϕ^s) across the signal polarisation ψ^s by weighting them with their SNR. This approximately accounts for the likelihood of the signal being detected. This SNR-averaged match is defined as,

$$\overline{M} = \left(\frac{\sum_i \rho_i^3 M_i^3}{\sum_i \rho_i^3} \right)^{1/3}, \quad (29)$$

where the sum is over all four signal polarisation values. So, for a given system, we have 750 values of the SNR averaged match. Using this set of match values and Eq. (28), we can then estimate the SNR (ρ_c) at which the proxy template could be distinguished from the signal.

In subsequent sections we will discuss our distinguishability results across each of the configurations in Tab. I, but in this section we will make some general comments on our results, and their accuracy.

We calculate the SNR-averaged match over all values of $(\theta^s, \phi^s, \psi^s)$, to estimate the average SNR at which two different configurations could be distinguished. As seen by the $\phi_{\text{Sn}} = 0$ template, the overall average match (\overline{M}) value with $\phi_{\text{Sn}} = \pi/2$ signal for the $q = 1$, $q = 2$ and $q = 4$ systems are 0.9981, 0.9983 and 0.9811 which translate to a ρ_c of 57, 60 and 17 respectively. Hence, on average, for high-spins, systems with varying in-plane spin directions can be distinguished at moderate SNRs.

As reported in Sec. II, the matches between the 80- and 96-point runs (for q2a07p0 and q2a07p90) are ~ 0.9995 - 0.99995 , which translates to ρ_c between 110 and 350. This suggests that we can identify two waveforms as indistinguishable up to SNRs of at least 110. We also computed the matches between the $\phi_{\text{Sn}} = 0, \pi/2$ systems using the corresponding 80- and 96-point waveforms over a range of (θ, ϕ) values, and found that the relative error between them is $O(0.05\%)$. These numbers suggest that although we should be cautious when interpreting very large values of ρ_c , we expect that the qualitative behaviour of the matches to remain unchanged with more accurate simulations.

When comparing our NR configurations, we expect a symmetry between systems with a ϕ_{Sn} difference of π . An in-plane spin rotation of π would correspond to flipping the direction of the out-of-plane recoil, and therefore we would expect that the signal from a ϕ_{Sn} system would be identical to that from a $\phi_{\text{Sn}} + \pi$ system if observed from the opposite side of the orbital plane, i.e., with $\theta \rightarrow \theta + \pi$. We verify this symmetry in Fig. 1, where we plot the ρ_c across signal θ for a range of signal ϕ for which M is computed with $(\theta_{\text{template}}, \phi_{\text{template}}) = (\theta_{\text{signal}} + \pi, \phi_{\text{signal}})$ and the match is optimized only over template ψ . The $\rho_c \geq 100$ for all $\phi_{\text{Sn}} = \pi$ signals for the $q = 1$ and $q = 2$ systems, with the $\rho_c \geq 50$ for every value of θ_{signal} for $q = 4$ system.

We do not observe an exact symmetry (i.e., a mismatch of zero), because in the $q = 1$ and $q = 4$ systems, we did not simply rotate the spin between each configuration, but instead calculated initial parameters individually for each value of ϕ_{Sn} , so these do not form a one-parameter family. Even when we have rotated the spin within a series, as in the $q = 2$ series, we have not changed the momenta; we would expect even lower mismatches if the out-of-plane momenta had been reflected in the orbital plane between the ϕ_{Sn} and $\phi_{\text{Sn}} + \pi$ configurations.

In Fig. 2 we plot the differences in the β Euler angle for these $q = 2$ and $q = 4$ systems. We can see that $\Delta\beta \sim 0$ for $q = 2$, but rises to a few $\sim O(1^\circ)$ for $q = 4$; this is consistent with our expectation that in the $q = 2$ series we have constructed configurations that better represent the symmetry. We note that in comparing the $\phi_{\text{Sn}} = 0$ and $\phi_{\text{Sn}} = \pi/2$ configurations, there is a clear difference in β during the merger and ringdown. Similar behaviour is seen for the other Euler angles (α, ϵ).

Fig. 3 shows contour plots the variation of ρ_c across the signal (θ, ϕ) for the q2a07p90 and q4a08p90 signals as seen by the q2a07p0 and q4a08p0 systems respectively, where the match at each (θ, ϕ) point is maximised over template (θ, ϕ, ψ) and then averaged over the signal ψ values using Eq. 29 and ρ_c is computed using Eq. 28. For the $q = 2$ system, $20 \lesssim \rho_c \lesssim 72$, whereas for the $q = 4$ system, $11 \lesssim \rho_c \lesssim 32$. Precession effects are more pronounced at edge-on than face-on inclination, so the lower ρ_c for q2a07p90 at $\theta \sim \pi/2$ is expected. For q4a08p90, this behaviour seems to reverse (higher ρ_c at edge-on compared to face-on). In Sec. VC, we remove the mode-asymmetry from the waveforms and compute the matches between the symmetrized waveforms for the $\phi_{\text{Sn}} = \pi/2$ signals as seen by $\phi_{\text{Sn}} = 0$ template. The contour plots from the symmetrized waveform results for the $q = 4$ system show a similar behaviour as for the $q = 2$ system, i.e., higher ρ_c for face-on/face-off signals vs. edge-on signals. This implies that the behaviour of ρ_c across the (θ, ϕ) space can be strongly affected by mode-asymmetric content for these $q = 4$ systems.

We see from Fig. 3 that there is a wide variation in the SNR at which these configurations would be distinguishable, depending on their orientation to the detector. In some cases, these signals would be distinguishable at low SNRs, and well within the SNRs of signals that have already been observed: the highest BBH SNR to date has been GW150914, with an SNR of ~ 24 [53]. To provide a better indication of the fraction of orientations over which these configurations would be distinguishable, in the following sections we find it more instructive to plot the relative percentage of total signals distinguishable at a given SNR for a given template (id2)–signal (id1) combination. So, we compute the quantity,

$$\Gamma(\rho) = 100 \frac{\text{len}(\mathcal{S}_{\text{id2:id1}}[\rho < \rho_c])}{\text{len}(\mathcal{S}_{\text{id2:id1}})}, \quad (30)$$

where $\mathcal{S}_{\text{id2:id1}}[\rho < \rho_c]$ is the list of SNRs with ρ less than a given ρ_c and $\mathcal{S}_{\text{id2:id1}}$ is the list of all the values.

V. RESULTS

We now consider in detail the distinguishability of our NR configurations.

In Sec. VA we compare the full NR waveforms (up to the $\ell = 2$ multipoles). This allows us to identify when configurations with different choices of ϕ_{Sn} will be distinguishable, and to compare this with the effect of changing the in-plane spin magnitude.

We then attempt to isolate the causes of these differences. In Sec. VB, we transform the waveforms into the co-precessing frame (where modes with $|m| < 2 \approx 0$) and study the matches between the waveform with symmetrized $(l, |m|) = (2, 2)$ modes for $\phi_{\text{Sn}} \pm \pi/2$ systems. This allows us to estimate the distinguishability of two waveforms when both precession and mode-asymmetry effects are muted, due primarily

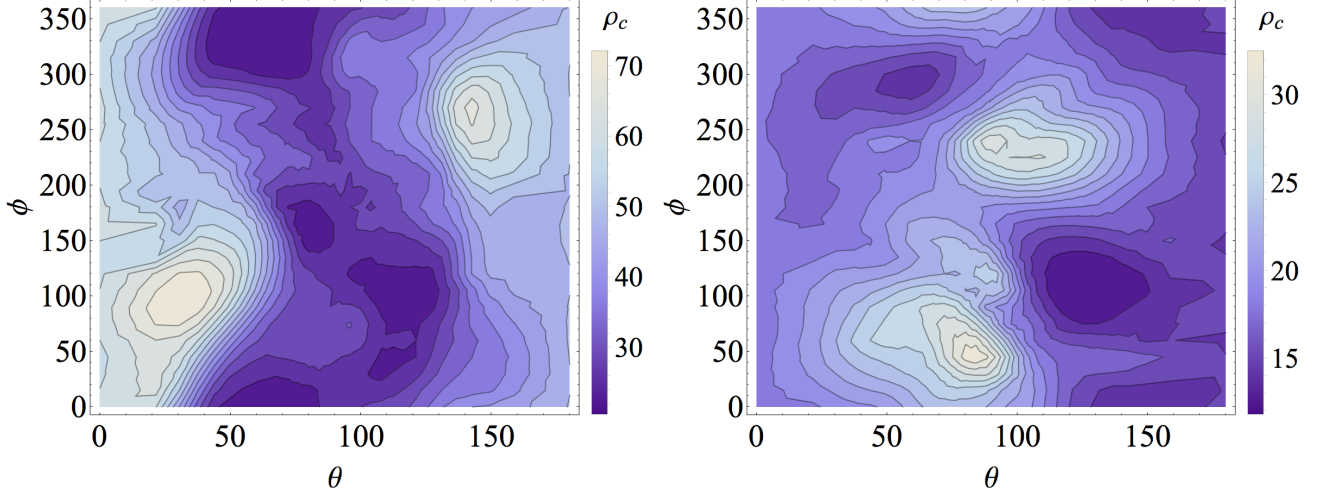


Figure 3. The left and right panels show the contour plot of ρ_c for the signal q2a07p90 and q4a08p90 as seen by template q2a07p0 and q4a08p0 respectively over the signal (θ, ϕ) values with the label on the right of each plot showing the values of ρ_c . See text for further discussion.

to small differences in the inspiral rate and merger-ringdown differences. These co-precessing-frame symmetrized modes are then transformed back to the inertial frame and Sec. VC presents the results of analysis with those waveforms. These results estimate the impact of neglecting mode-asymmetry on the distinguishability of precessing-binary waveforms.

A. Full waveform analysis

The key results of this work are shown in Fig. 4. In the upper panel we plot $\Gamma(\rho)$ calculated between the $\phi_{\text{Sn}} = 0$ and $\phi_{\text{Sn}} = \pi/2$ simulations, for $q = 1, 2, 4$. The figure shows the percentage of signals that will be distinguishable with the $\phi_{\text{Sn}} = 0$ template below a given SNR. The annotation “Full” in the legend (and all other plots hence) indicates that we are using all of the $\ell = 2$ information in the NR waveform in the inertial frame without symmetrizing the modes.

For the $q = 1$ super-kick configurations, the detectability between $\phi_{\text{Sn}} \pm \pi/2$ systems is due to asymmetric radiation of gravitational modes. The detectable SNRs for these super-kick systems, ($45 \lesssim \rho_c \lesssim 80$), are in the possible range of ground based detectors, but will be rare; we expect less than one in every hundred signals to have such high SNRs. The recoil velocities for the $q = 1$ waveforms used here are ~ 700 km/s ($\phi_{\text{Sn}} = 0$) and ~ 2700 km/s ($\phi_{\text{Sn}} = \pi/2$). For systems with lower spins (and hence lower recoil velocities), we can expect larger values of ρ_c , meaning that these differences will be more difficult to measure. These results are consistent with those presented in Refs. [54, 55].

The ρ_c for the $q = 2$ systems with $\phi_{\text{Sn}} = 0, \pi/2$ are in the range of $20 \lesssim \rho_c \lesssim 75$, and for $q = 4$ they are $12 \lesssim \rho_c < 35$. Given that GW signals have already been observed with SNRs as high as 30 [56], and the detection threshold is at an SNR of approximately 10, these are well within the range of current ground-based detectors. We emphasize that these results do not mean we can necessarily measure, for example, the spin direction at the frequency when the signal enters the detector’s sensitivity band; this quantity may be degenerate with other physical properties. However, they do indicate that sys-

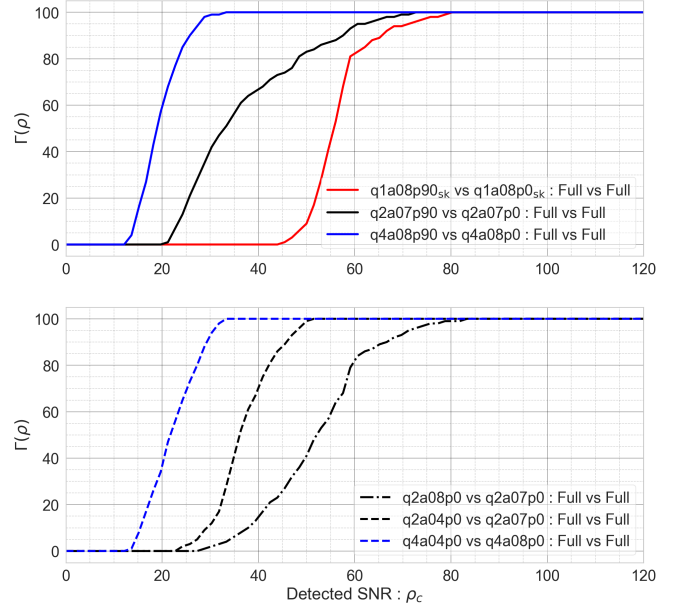


Figure 4. $\Gamma(\rho)$ as defined in Eq. (30). Top panel: $q = 1, 2, 4$ systems with ϕ_{Sn} differences of $\pi/2$. Lower panel: $q = 2, 4$ systems with different spin values. The results for $q = 1$, $q = 2$ and $q = 4$ are shown in Red, Black and Blue respectively. The solid lines show the results for systems with ϕ_{Sn} differences of $\pi/2$ and the same χ_p , the dashed-lines show the results for large χ_p differences (0.3 for $q = 2$ and 0.4 for $q = 4$) with the same ϕ_{Sn} , and the dotted-dashed for small χ_p differences (0.1 for $q = 2$) with the same ϕ_{Sn} . See text for further details.

tems with different values of ϕ_{Sn} can be distinguished from each other, and if we do not take into account the effects on the waveform of varying ϕ_{Sn} (as in current Phenom and EOB models), then these differences will manifest themselves in biases in at least one physical parameter.

We might expect that the effect of ϕ_{Sn} on measurements will be far smaller than that of the spin magnitude. The lower panel of Fig. 4 shows that this is not necessarily the case. When comparing the $q = 2$ configurations with χ_p values of 0.7 and

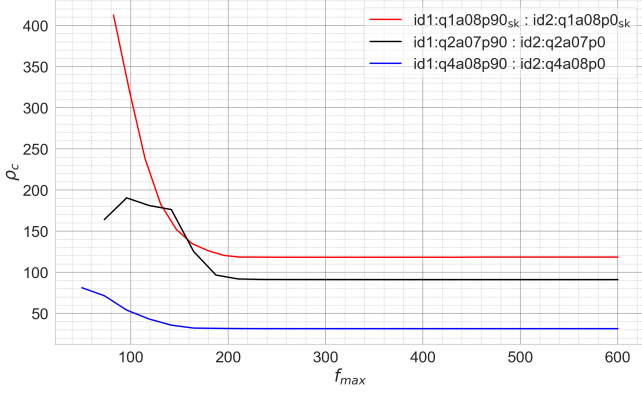


Figure 5. This plot shows the ρ_c computed from the match (\mathcal{M}) between the symmetrized QA frame waveforms for the $q = 2$, $q = 4$ systems (solid-black, solid-blue respectively) and symmetrized $q = 1$ waveforms (solid-red), for varying values of the upper cutoff frequency in f_{\max} in the match calculation.

0.8, we find that they will be distinguishable for SNRs in the range $30 \lesssim \rho_c \lesssim 80$. A change in the spin of 0.1 is therefore in general more difficult to distinguish than a change in the in-plane spin direction of $\pi/2$. A change in the spin magnitude of 0.3 (between the $q = 2$ 0.7 and 0.4 configurations) is distinguishable at SNRs in the range $25 \lesssim \rho_c \lesssim 45$. As we can see by comparing with the upper panel, this is comparable to the distinguishability of a spin rotation of $\pi/2$. In the $q = 4$ configurations, we see that a spin change of 0.4 (between 0.8 and 0.4) is distinguishable in the SNR range $13 \lesssim \rho_c < 35$, again comparable to what we see for a spin rotation. These results suggest that the SNRs at which in-plane spin magnitudes become measurable are also the SNRs at which changes in the waveform due to spin rotations also become measurable. As noted above, this study cannot tell us which physical measurements will be biased by models that neglect mode asymmetries or changes in the binary dynamics, but our results raise the possibility that accurate measurements of precessing systems, i.e., of black-hole spins, will not be possible without the inclusion of some or all of these effects in waveform models.

For the $q = 2$ and $q = 4$ systems with different spin directions, we observe a slight difference in the merger times, mode-asymmetric content as well as precessional dynamics (as can be seen from the $\Delta\beta$ plot in Fig. 2). These differences are the main reason for distinguishability of systems with different spin directions. These effects will become weaker for lower spins, but one should bear in mind that precession effects and black-hole spins will also become more difficult to measure [1]. As such, we expect these results to be largely independent of spin magnitude. A more important caveat on these results is that they are restricted to signals of total mass of $100 M_\odot$. For lower-mass systems we expect the mode asymmetries to contribute less to the SNR, and therefore to have less impact. We leave a study of the impact of mode asymmetries on parameter measurements to future work.

B. QA frame symmetrized waveform analysis

As mentioned previously, for the $q = 2$ and $q = 4$ systems

with different ϕ_{Sn} , the mismatches are due not only to differences in their mode-asymmetric content, but also differences in the precessional motion (i.e., differences in the $(\alpha, \beta, \epsilon)$ angles) and differences in their inspiral rate. In this section our aim is to remove as much as possible the precession and mode-asymmetry effects, and to quantify the impact of all other effects. We transform the $q = 2$ and $q = 4$ waveforms into the co-precessing frame (specifically, the quadrupole-aligned, “QA”, frame [26–28]) using Eq. (3). This minimises modulations due to precession. In this frame the dominant power is in the $(\ell = 2, |m| = 2)$ harmonics. We then symmetrise these harmonics, to remove the effects of mode asymmetries. In terms of the QA frame modes ($h_{\ell m}^{\text{QA}}$), the symmetric waveform in the QA frame ($h_{22}^{\text{QA, symm}}$) is defined as,

$$h_{22}^{\text{QA, symm}} = \frac{1}{2} (h_{22}^{\text{QA}} + h_{2,-2}^{*\text{QA}}), \quad (31)$$

where $h_{\ell m}^*$ is the complex conjugate of the mode. Using this, we can define the $(2, -2)$ mode as, $h_{2,-2}^{\text{QA, symm}} = h_{2,2}^{*\text{QA, symm}}$, using the relation $h_{\ell m} = (-1)^\ell h_{\ell, -m}^*$. Doing this for the $q = 2$ and $q = 4$ systems removes the precession modulations and mode-asymmetry. As the super-kick simulations are non-precessing, those waveforms are symmetrized in the inertial frame using Eq. (31).

Matches calculated between symmetrized QA $(2, 2)$ modes are independent of orientation and polarisation, so the averaging that we performed previously is no longer necessary. Between the $\phi_{\text{Sn}} \pm \pi/2$ configurations at mass ratios $q = 1, 2, 4$, the indistinguishability SNRs are now 120, 90 and 30, respectively. If we contrast these with the top panel of Fig. 4, we see that for the $q = 2$ and $q = 4$ cases, differences in the signal phase make a noticeable contribution to the indistinguishability SNR. In Fig. 5 we show ρ_c over a range of f_{\max} values. Fig. 6 shows the $q = 2$ series waveforms in time and frequency domain, to illustrate where these choices of f_{\max} occur during the binaries’ coalescence. These figures show that, as we might expect, most of the disagreement between the waveforms accumulates during merger and ringdown.

These results should be taken with a few caveats. As already mentioned, for the $q = 2$ waveforms obtained with 80- and 96-point resolutions, over the θ space, the match lies between 0.9995 - 0.99995 which translates to ρ_c of $\sim 110 - 345$. So, although the QA frame symmetrized matches are close to the minimum match due to NR uncertainties, over the majority of the θ space, the QA frame symmetrized results should hold even for more accurate NR waveforms. For the $q = 4$ system, to obtain the low eccentricity parameters, the momenta between the $\phi_{\text{Sn}} = 0, \pi/2$ systems are slightly different, which could be one of the sources of disagreement between the QA-frame symmetrized waveforms. However, the similarity of the trends of the match vs f_{\max} for all three systems indicate that the above results should hold within these uncertainties.

C. Inertial frame symmetrized waveform analysis

We now transform the symmetrized QA frame waveforms to the inertial frame using Eq. (3) and the corresponding $(\alpha, \beta, \epsilon)$ angles for each system. This is similar to how current waveform models construct the precessing waveforms in

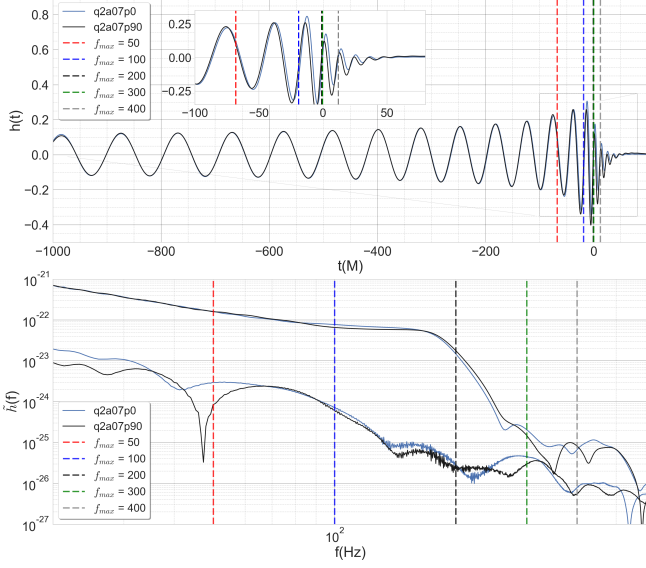


Figure 6. In the top [bottom] panel, we plot the q2a07p0 (blue) and q2a07p90 (black) time [frequency] domain QA frame symmetrized waveforms. For the top panel, the dashed lines show the time at which the waveform has a specific frequency used as f_{\max} value for Fig. 5. For the bottom panel, the dashed lines show the position of that frequency with respect to the frequency domain waveform. Frequency values of (50, 100, 200, 300, 400) are given in dashed (red, blue, black, green, gray) lines respectively.

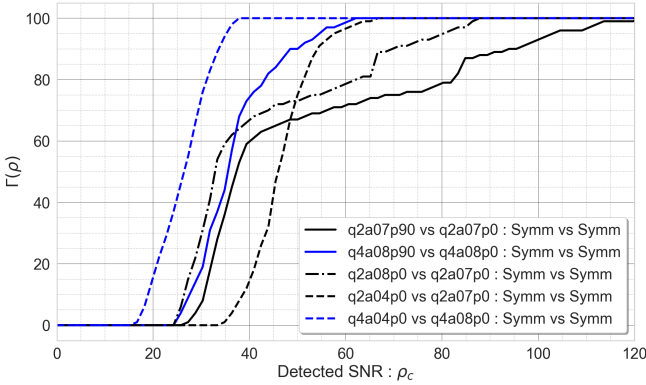


Figure 7. $\Gamma(\rho)$ for the systems q2a07p90 (solid-black), q2a08p0 (dashed-dotted -black), q2a04p0 (dashed-black) matched with the q2a07p0 proxy template. The q4a08p90 and q4a04p0 systems matched with q4a08p0 template are shown by solid-blue and dashed-blue respectively. The legend naming follows the convention, “signal waveform vs template waveform : signal effects vs template effects”, where “Symm” means the waveform is symmetrized in the QA frame and transformed back to inertial frame.

the inertial frame, i.e., they transform a model for the corresponding aligned-spin QA frame waveform to the inertial frame using a model for the precession Euler angles. Using these waveforms, we perform the same analysis as in Sec. V A and plot the $\Gamma(\rho)$ quantity in Fig. 7. Note, that for the $q = 1$ system, the symmetrized waveform matches will be the same as presented in Fig. 5 and we will not discuss that system here.

We consider first the two $\phi_{\text{Sn}} = 0, \pi/2$ comparisons, which are for the $q = 2$ and $q = 4$ configurations. Between the symmetrized q2a07 systems, the distinguishability SNR is

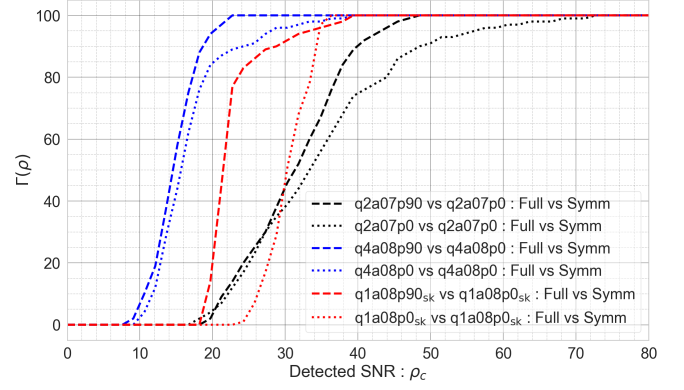


Figure 8. $\Gamma(\rho)$ for the $q = 1$, $q = 2$ and $q = 4$ systems plotted in Red, Black and Blue respectively. Here, the full waveform $\phi_{\text{Sn}} = \pi/2$ signal and $\phi_{\text{Sn}} = 0$ signal as seen by the symmetrized $\phi_{\text{Sn}} = 0$ template are shown by the dashed and dotted lines respectively. The legend naming follows the convention, “signal simulation vs template simulation : signal effects vs template effects”, where “Symm” means the waveform is symmetrized in QA frame and transformed back to inertial frame and “Full” means waveform with both precession and mode-asymmetry effects.

$25 \lesssim \rho_c \lesssim 115$. Between the symmetrized q4a08 systems, the distinguishability SNR is $25 \lesssim \rho_c \lesssim 60$. In both cases, this is significantly higher than for the full waveforms, and the range is either side of the value for the symmetrized QA waveforms. In particular, we see that the presence of asymmetries makes the q2a07 cases distinguishable at SNRs as low as 20, and the q4a08 cases distinguishable at SNRs as low as 10, while, if the asymmetries did not exist, they would not be distinguishable for SNRs lower than ~ 30 .

If we now consider the distinguishability between configurations with different spin magnitudes, comparing Figs. 4 and 7, we see a similar effect. Although for $q = 2$ configurations the ρ_c for different spin values shows an overall increase, a few of the signals with a χ_p difference of 0.1 are now easier to distinguish than a χ_p difference of 0.3. The most pronounced effect is for $q = 4$ configurations, where the spin difference of 0.4 is now easier to distinguish than the rotation of the spin.

Neither of the previous analyses reflects the scenario of current GW measurements, where the signals correspond to “full” waveforms, and they are analysed using models that correspond approximately to the symmetrized waveforms of the previous analysis. In an attempt to estimate the impact of using symmetrized models in analysis, Fig. 8 shows $\Gamma(\rho)$ for the $\phi_{\text{Sn}} = 0, \pi/2$ full waveform signals matched against the symmetrized inertial frame $\phi_{\text{Sn}} = 0$ templates for the $q = 1$, $q = 2$ and $q = 4$ simulations. We observe that for $\phi_{\text{Sn}} = \pi/2$, it is generally easier for the symmetrized template to distinguish the signal as compared to the full waveform templates. This effect is very strong for the $q = 1$ super-kick cases where the distinguishability SNR reduces by almost 20 for all signals. We also see that removing the mode-asymmetric content leads to large mis-matches between waveforms of the same systems causing the symmetrized $\phi_{\text{Sn}} = 0$ template to be distinguishable from the full waveform $\phi_{\text{Sn}} = 0$ signal at moderate ($10 < \rho_c < 40$) SNRs for all mass ratios. All these results indicate that the absence of mode asymmetries in current models will lead to measurement biases in these systems. We expect that even for comparable-mass systems, if the to-

Signal	Template	Signal Effects	Template Effects	Average Match	ρ_c
q2a07p90	q2a07p0	Full	Full	0.9983	60
q2a07p90	q2a07p0	Symmetrized	Symmetrized	0.9991	83
q2a07p90	q2a07p0	Full	Symmetrized	0.9954	36
q2a07p0	q2a07p0	Full	Symmetrized	0.9969	44
q2a08p0	q2a07p0	Full	Full	0.9983	60
q2a08p0	q2a07p0	Symmetrized	Symmetrized	0.9986	65
q2a04p0	q2a07p0	Full	Full	0.9952	36
q2a04p0	q2a07p0	Symmetrized	Symmetrized	0.9969	44
q4a08p90	q4a08p0	Full	Full	0.9811	18
q4a08p90	q4a08p0	Symmetrized	Symmetrized	0.9935	30
q4a08p90	q4a08p0	Full	Symmetrized	0.9737	15
q4a08p0	q4a08p0	Full	Symmetrized	0.9785	16
q4a04p0	q4a08p0	Full	Full	0.9936	30
q4a04p0	q4a08p0	Symmetrized	Symmetrized	0.9942	32
q1a08p90	q1a08p0	Full	Full	0.9981	57
q1a08p90	q1a08p0	Full	Symmetrized	0.9882	22
q1a08p0	q1a08p0	Full	Symmetrized	0.9934	30

Table II. The SNR averaged match, Eq. (29), over all the (θ, ϕ, ψ) values for the systems considered in this study. From left to right, the columns state the signal waveform configuration, template waveform configuration, signal effects (full waveform or symmetrized), template effects (full waveform or symmetrized), average match value and corresponding SNR respectively, using Eq. (28). See text for further discussion.

tal mass is high ($> 100 M_\odot$) and the in-plane spins are high, systematic errors are likely to be significant.

In Tab. II, we list the SNR averaged match values over all the signal (θ, ϕ, ψ) values to provide one single number for the distinguishability of the signal. We can see that when both signal and templates are symmetrized, for all systems, the agreement between the waveforms increases leading to larger distinguishability SNR. When symmetrized waveform templates are matched with full waveform signals, we see an overall decrease in the distinguishability SNR. Even when both the signal and template systems are the same, with symmetrized templates, ρ_c is comparable to that of $\phi_{\text{Sn}} \pm \pi/2$ results.

VI. CONCLUSIONS

We have investigated when changes in the in-plane spin direction of binary-black-hole systems, the effects of which are not included in current Phenom and EOB models, will be distinguishable in GW measurements. To do that, we use a set of NR simulations obtained from the BAM code (see Tab. I). We quantify the distinguishability of systems with different choices of in-plane spin direction ϕ_{Sn} by calculating matches between them. This approach allows us to calculate the SNR at which the signals will be distinguishable. Our study is restricted to a small number of configurations at mass ratios $q = 1, 2, 4$, and large in-plane spin magnitudes of 0.7 and 0.8, with two configurations with moderate in-plane spin of 0.4. All of our calculations are performed on systems with total mass $100 M_\odot$.

Changes in ϕ_{Sn} have several effects on the binary dynamics and the waveform. One effect that we discuss in detail is an asymmetry between the $\pm m$ waveform modes. Another is

small changes in the phasing of the binary, and in the merger and ringdown signal. By removing asymmetry and/or precession effects from our waveforms, we show that all of these effects contribute to the waveform variations between different choices of ϕ_{Sn} . When mode-asymmetries are muted, the distinguishability SNR ρ_c for *all* the systems (different ϕ_{Sn} and different χ_p) show a marked increase across the (θ, ϕ) space (see Fig. 7). Disregarding mode asymmetries increases ρ_c by factors of $\sim 1.5 - 1.9$ between systems of different ϕ_{Sn} , indicating that this is a significant feature of these waveforms.

Our main results are shown in Sec. V A, and show that for large in-plane spins, variations in ϕ_{Sn} will be distinguishable at moderate SNRs. More importantly, these effects will influence measurements at SNRs comparable to those at which in-plane spin magnitudes become measurable. For example, in the $q = 2$ systems we considered, a change in spin magnitude of 0.3 will be distinguishable at a comparable SNR to a change in spin direction of $\pi/2$. This effect will be reduced for smaller spins, but so will our ability to measure the spin magnitude. Precession effects and in-plane spin magnitude, typically captured by the parameter χ_p , have not yet been identified in individual observations [1]. Our results suggest that when they are, the absence of in-plane spin direction effects in the modelling could lead to significant parameter biases. We plan to study the impact on parameter estimation in future work.

There are a number of questions that require further work. We have limited ourselves to small number of configurations, and to one choice of total mass. We have also neglected the effect of $\ell > 2$ modes, which also impact parameter estimation for systems with mass ratios of $q \geq 2$ [57]. The impact of changes in ϕ_{Sn} , and the importance of mode asymmetries, also needs to be studied for systems with lower masses, where the inspiral contributes more power to the waveform, with mode-asymmetric effects being weaker but with a larger number of precessional cycles. However, in order to fully understand the importance of these physical effects, we require models that include them, which can then be used in parameter-estimation studies. This work has provided strong evidence that these effects must be taken into account in order to make unbiased physical measurements from GW observations, and therefore already provide a strong motivation for such modelling. This has already been done for the surrogate models described in Refs. [58, 59]. Since these models are valid only for high-mass systems and a limited range of mass ratios, it would be advantageous to be extended to other classes of model.

VII. ACKNOWLEDGEMENTS

We thank Frank Ohme and Sebastian Khan for useful discussions. We thank Edward Fauchon-Jones, Eleanor Hamilton, Charlie Hoy and Dave Yeeles for their help in performing the comparison cases NR simulations.

This work was supported by Science and Technology Facilities Council (STFC) grant ST/L000962/1, European Research Council Consolidator Grant 647839. We are grateful for computational resources provided by Cardiff University, and funded by an STFC grant supporting UK Involvement in the Operation of Advanced LIGO.

Numerical simulations were performed on the DiRAC@Durham facility managed by the Institute for

Computational Cosmology on behalf of the STFC DiRAC HPC Facility (www.dirac.ac.uk). The equipment was funded by BEIS capital funding via STFC capital grants

ST/P002293/1, ST/R002371/1 and ST/S002502/1, Durham University and STFC operations grant ST/R000832/1. DiRAC is part of the National e-Infrastructure.

-
- [1] S. Fairhurst, R. Green, M. Hannam, and C. Hoy, “When will we observe binary black holes precessing?,” 8 2019.
 - [2] J. Aasi *et al.*, “Advanced LIGO,” *Class. Quant. Grav.*, vol. 32, p. 074001, 2015.
 - [3] F. Acernese *et al.*, “Advanced Virgo: a second-generation interferometric gravitational wave detector,” *Class. Quant. Grav.*, vol. 32, no. 2, p. 024001, 2015.
 - [4] B. P. Abbott *et al.*, “GWTC-1: A Gravitational-Wave Transient Catalog of Compact Binary Mergers Observed by LIGO and Virgo during the First and Second Observing Runs,” 2018.
 - [5] A. H. Nitz, T. Dent, G. S. Davies, S. Kumar, C. D. Capano, I. Harry, S. Mozzon, L. Nuttall, A. Lundgren, and M. Tápai, “2-OGC: Open gravitational-wave catalog of binary mergers from analysis of public advanced LIGO and virgo data,” *The Astrophysical Journal*, vol. 891, p. 123, mar 2020.
 - [6] B. Zackay, L. Dai, T. Venumadhav, J. Roulet, and M. Zaldarriaga, “Detecting Gravitational Waves With Disparate Detector Responses: Two New Binary Black Hole Mergers,” 10 2019.
 - [7] T. Venumadhav, B. Zackay, J. Roulet, L. Dai, and M. Zaldarriaga, “New binary black hole mergers in the second observing run of Advanced LIGO and Advanced Virgo,” *Phys. Rev. D*, vol. 101, no. 8, p. 083030, 2020.
 - [8] R. Abbott *et al.*, “GW190814: Gravitational Waves from the Coalescence of a 23 Solar Mass Black Hole with a 2.6 Solar Mass Compact Object,” *Astrophys. J.*, vol. 896, no. 2, p. L44, 2020.
 - [9] R. Abbott *et al.*, “GW190412: Observation of a Binary-Black-Hole Coalescence with Asymmetric Masses,” 4 2020.
 - [10] B. Abbott *et al.*, “GW190425: Observation of a Compact Binary Coalescence with Total Mass $\sim 3.4M_{\odot}$,” *Astrophys. J. Lett.*, vol. 892, no. 1, p. L3, 2020.
 - [11] B. Abbott *et al.*, “Binary Black Hole Population Properties Inferred from the First and Second Observing Runs of Advanced LIGO and Advanced Virgo,” *Astrophys. J. Lett.*, vol. 882, no. 2, p. L24, 2019.
 - [12] S. Khan, S. Husa, M. Hannam, F. Ohme, M. Pürrer, X. Jiménez Forteza, and A. Bohé, “Frequency-domain gravitational waves from nonprecessing black-hole binaries. II. A phenomenological model for the advanced detector era,” *Phys. Rev.*, vol. D93, no. 4, p. 044007, 2016.
 - [13] L. London, S. Khan, E. Fauchon-Jones, C. García, M. Hannam, S. Husa, X. Jiménez-Forteza, C. Kalaghatgi, F. Ohme, and F. Pannarale, “First higher-multipole model of gravitational waves from spinning and coalescing black-hole binaries,” *Phys. Rev. Lett.*, vol. 120, no. 16, p. 161102, 2018.
 - [14] M. Hannam, P. Schmidt, A. Bohé, L. Haegel, S. Husa, F. Ohme, G. Pratten, and M. Pürrer, “Simple Model of Complete Precessing Black-Hole-Binary Gravitational Waveforms,” *Phys. Rev. Lett.*, vol. 113, no. 15, p. 151101, 2014.
 - [15] S. Khan, K. Chatziioannou, M. Hannam, and F. Ohme, “Phenomenological model for the gravitational-wave signal from precessing binary black holes with two-spin effects,” *Phys. Rev.*, vol. D100, no. 2, p. 024059, 2019.
 - [16] A. Bohé *et al.*, “Improved effective-one-body model of spinning, nonprecessing binary black holes for the era of gravitational-wave astrophysics with advanced detectors,” *Phys. Rev.*, vol. D95, no. 4, p. 044028, 2017.
 - [17] R. Cotesta, A. Buonanno, A. Bohé, A. Taracchini, I. Hinder, and S. Ossokine, “Enriching the Symphony of Gravitational Waves from Binary Black Holes by Tuning Higher Harmonics,” *Phys. Rev.*, vol. D98, no. 8, p. 084028, 2018.
 - [18] Y. Pan, A. Buonanno, A. Taracchini, L. E. Kidder, A. H. Mroué, H. P. Pfeiffer, M. A. Scheel, and B. Szilágyi, “Inspiraling-down waveforms of spinning, precessing black-hole binaries in the effective-one-body formalism,” *Phys. Rev.*, vol. D89, no. 8, p. 084006, 2014.
 - [19] S. Babak, A. Taracchini, and A. Buonanno, “Validating the effective-one-body model of spinning, precessing binary black holes against numerical relativity,” *Phys. Rev.*, vol. D95, no. 2, p. 024010, 2017.
 - [20] A. Taracchini *et al.*, “Effective-one-body model for black-hole binaries with generic mass ratios and spins,” *Phys. Rev.*, vol. D89, no. 6, p. 061502, 2014.
 - [21] A. Ramos-Buades, P. Schmidt, G. Pratten, and S. Husa, “Validity of common modeling approximations for precessing binary black holes with higher-order modes,” *Phys. Rev. D*, vol. 101, no. 10, p. 103014, 2020.
 - [22] F. Herrmann, I. Hinder, D. Shoemaker, P. Laguna, and R. A. Matzner, “Gravitational recoil from spinning binary black hole mergers,” *Astrophys. J.*, vol. 661, pp. 430–436, 2007.
 - [23] C. García-Quirós, M. Colleoni, S. Husa, H. Estellés, G. Pratten, A. Ramos-Buades, M. Mateu-Lucena, and R. Jaume, “IMR-PhenomXHM: A multi-mode frequency-domain model for the gravitational wave signal from non-precessing black-hole binaries,” 1 2020.
 - [24] S. Ossokine *et al.*, “Multipolar Effective-One-Body Waveforms for Precessing Binary Black Holes: Construction and Validation,” 4 2020.
 - [25] S. Khan, F. Ohme, K. Chatziioannou, and M. Hannam, “Including higher order multipoles in gravitational-wave models for precessing binary black holes,” *Phys. Rev. D*, vol. 101, no. 2, p. 024056, 2020.
 - [26] P. Schmidt, M. Hannam, and S. Husa, “Towards models of gravitational waveforms from generic binaries: A simple approximate mapping between precessing and non-precessing inspiral signals,” *Phys. Rev.*, vol. D86, p. 104063, 2012.
 - [27] M. Boyle, R. Owen, and H. P. Pfeiffer, “A geometric approach to the precession of compact binaries,” *Phys. Rev.*, vol. D84, p. 124011, 2011.
 - [28] R. O’Shaughnessy, B. Vaishnav, J. Healy, Z. Meeks, and D. Shoemaker, “Efficient asymptotic frame selection for binary black hole spacetimes using asymptotic radiation,” *Phys. Rev.*, vol. D84, p. 124002, 2011.
 - [29] L. E. Kidder, “Coalescing binary systems of compact objects to (post)^{5/2}-newtonian order. v. spin effects,” *Phys. Rev. D*, vol. 52, pp. 821–847, Jul 1995.
 - [30] B. Bruegmann, J. A. Gonzalez, M. Hannam, S. Husa, and U. Sperhake, “Exploring black hole superkicks,” *Phys. Rev.*, vol. D77, p. 124047, 2008.
 - [31] R. O’Shaughnessy, L. London, J. Healy, and D. Shoemaker, “Precession during merger: Strong polarization changes are observationally accessible features of strong-field gravity during binary black hole merger,” *Phys. Rev. D*, vol. 87, no. 4, p. 044038, 2013.
 - [32] L. Pekowsky, R. O’Shaughnessy, J. Healy, and D. Shoemaker, “Comparing gravitational waves from nonprecessing and precessing black hole binaries in the corotating frame,” *Phys. Rev. D*, vol. 88, no. 2, p. 024040, 2013.
 - [33] M. Boyle, L. E. Kidder, S. Ossokine, and H. P. Pfeiffer, “Gravitational-wave modes from precessing black-hole binaries,” 2014.
 - [34] M. Campanelli, C. O. Lousto, Y. Zlochower, and D. Mer-

- ritt, “Maximum gravitational recoil,” *Phys. Rev. Lett.*, vol. 98, p. 231102, 2007.
- [35] J. A. Gonzalez, M. D. Hannam, U. Sperhake, B. Bruegmann, and S. Husa, “Supermassive recoil velocities for binary black-hole mergers with antialigned spins,” *Phys. Rev. Lett.*, vol. 98, p. 231101, 2007.
- [36] S. Husa, J. A. González, M. Hannam, B. Brügmann, and U. Sperhake, “Reducing phase error in long numerical binary black hole evolutions with sixth-order finite differencing,” *Classical and Quantum Gravity*, vol. 25, p. 105006, may 2008.
- [37] B. Brügmann, J. A. González, M. Hannam, S. Husa, U. Sperhake, and W. Tichy, “Calibration of moving puncture simulations,” *Phys. Rev. D*, vol. 77, p. 024027, Jan 2008.
- [38] P. Schmidt, F. Ohme, and M. Hannam, “Towards models of gravitational waveforms from generic binaries II: Modelling precession effects with a single effective precession parameter,” *Phys. Rev.*, vol. D91, no. 2, p. 024043, 2015.
- [39] M. Hannam, S. Husa, F. Ohme, D. Muller, and B. Bruegmann, “Simulations of black-hole binaries with unequal masses or nonprecessing spins: Accuracy, physical properties, and comparison with post-Newtonian results,” *Phys. Rev. D*, vol. 82, p. 124008, 2010.
- [40] S. Husa, S. Khan, M. Hannam, M. Pürrer, F. Ohme, X. Jiménez Forteza, and A. Bohé, “Frequency-domain gravitational waves from nonprecessing black-hole binaries. I. New numerical waveforms and anatomy of the signal,” *Phys. Rev.*, vol. D93, no. 4, p. 044006, 2016.
- [41] E. Fauchon-Jones, C. Kalaghatgi, E. Hamilton, D. Yeeles, C. Hoy, M. Hannam, A. Vano-Vinuales, J. Thompson, L. T. London, and S. Khan, “Bam catalogue of binary black hole simulations,” 2020, In preparation.
- [42] M. Pürrer, S. Husa, and M. Hannam, “An Efficient iterative method to reduce eccentricity in numerical-relativity simulations of compact binary inspiral,” *Phys. Rev. D*, vol. 85, p. 124051, 2012.
- [43] S. Husa, M. Hannam, J. A. González, U. Sperhake, and B. Brügmann, “Reducing eccentricity in black-hole binary evolutions with initial parameters from post-newtonian inspiral,” *Phys. Rev. D*, vol. 77, p. 044037, Feb 2008.
- [44] E. Baird, S. Fairhurst, M. Hannam, and P. Murphy, “Degeneracy between mass and spin in black-hole-binary waveforms,” *Phys. Rev. D*, vol. 87, no. 2, p. 024035, 2013.
- [45] E. E. Flanagan and S. A. Hughes, “Measuring gravitational waves from binary black hole coalescences: 2. The Waves’ information and its extraction, with and without templates,” *Phys. Rev. D*, vol. 57, pp. 4566–4587, 1998.
- [46] L. Lindblom, B. J. Owen, and D. A. Brown, “Model Waveform Accuracy Standards for Gravitational Wave Data Analysis,” *Phys. Rev. D*, vol. 78, p. 124020, 2008.
- [47] S. T. McWilliams, B. J. Kelly, and J. G. Baker, “Observing mergers of non-spinning black-hole binaries,” *Phys. Rev. D*, vol. 82, p. 024014, 2010.
- [48] H.-S. Cho, E. Ochsner, R. O’Shaughnessy, C. Kim, and C.-H. Lee, “Gravitational waves from black hole-neutron star binaries: Effective Fisher matrices and parameter estimation using higher harmonics,” *Phys. Rev. D*, vol. 87, no. 2, p. 024004, 2013.
- [49] K. Chatziioannou, A. Klein, N. Yunes, and N. Cornish, “Constructing Gravitational Waves from Generic Spin-Precessing Compact Binary Inspirals,” *Phys. Rev.*, vol. D95, no. 10, p. 104004, 2017.
- [50] M. Pürrer and C.-J. Haster, “Ready for what lies ahead? – Gravitational waveform accuracy requirements for future ground based detectors,” *Phys. Rev. Res.*, vol. 2, no. 2, p. 023151, 2020.
- [51] I. Harry, J. Calderón Bustillo, and A. Nitz, “Searching for the full symphony of black hole binary mergers,” *Phys. Rev.*, vol. D97, no. 2, p. 023004, 2018.
- [52] A. Buonanno, Y.-b. Chen, and M. Vallisneri, “Detecting gravitational waves from precessing binaries of spinning compact objects: Adiabatic limit,” *Phys. Rev.*, vol. D67, p. 104025, 2003. [Erratum: *Phys. Rev. D* 74, 029904(2006)].
- [53] B. Abbott *et al.*, “Binary Black Hole Mergers in the first Advanced LIGO Observing Run,” *Phys. Rev. X*, vol. 6, no. 4, p. 041015, 2016. [Erratum: *Phys. Rev. X* 8, 039903 (2018)].
- [54] V. Varma, M. Isi, and S. Biscoveanu, “Extracting the Gravitational Recoil from Black Hole Merger Signals,” *Phys. Rev. Lett.*, vol. 124, no. 10, p. 101104, 2020.
- [55] C. O. Lousto and J. Healy, “Kicking gravitational wave detectors with recoiling black holes,” *Phys. Rev.*, vol. D100, no. 10, p. 104039, 2019.
- [56] B. Abbott *et al.*, “GW170817: Observation of Gravitational Waves from a Binary Neutron Star Inspiral,” *Phys. Rev. Lett.*, vol. 119, no. 16, p. 161101, 2017.
- [57] C. Kalaghatgi, M. Hannam, and V. Raymond, “Parameter estimation with a spinning multimode waveform model,” *Phys. Rev. D*, vol. 101, no. 10, p. 103004, 2020.
- [58] J. Blackman, S. E. Field, M. A. Scheel, C. R. Galley, C. D. Ott, M. Boyle, L. E. Kidder, H. P. Pfeiffer, and B. Szilágyi, “Numerical relativity waveform surrogate model for generically precessing binary black hole mergers,” *Phys. Rev.*, vol. D96, no. 2, p. 024058, 2017.
- [59] V. Varma, S. E. Field, M. A. Scheel, J. Blackman, D. Gerosa, L. C. Stein, L. E. Kidder, and H. P. Pfeiffer, “Surrogate models for precessing binary black hole simulations with unequal masses,” 2019.